PROCEEDINGS A

royalsocietypublishing.org/journal/rspa

Research

Cite this article: Kumar A, Handral P, Bhandari D, Rangarajan R. 2021 More views of a one-sided surface: mechanical models and stereo vision techniques for Möbius strips. *Proc. R. Soc. A* **477**: 20210076. https://doi.org/10.1098/rspa.2021.0076

Received: 1 February 2021
Accepted: 13 May 2021

Subject Areas:
experimental mechanics, computer vision, mechanical engineering

Keywords:
elastic ribbons, nonlinear rods, Wunderlich model, Cosserat plates, computer vision, experimental validation

Author for correspondence:
Ramsharan Rangarajan
e-mail: rram@iisc.ac.in

More views of a one-sided surface: mechanical models and stereo vision techniques for Möbius strips

Arun Kumar, Poornakanta Handral, Darshan Bhandari and Ramsharan Rangarajan

Department of Mechanical Engineering, Indian Institute of Science Bangalore, India

RR, 0000-0001-7403-7728

Möbius strips are prototypical examples of ribbon-like structures. Inspecting their shapes and features provides useful insights into the rich mechanics of elastic ribbons. Despite their ubiquity and ease of construction, quantitative experimental measurements of the three-dimensional shapes of Möbius strips are surprisingly non-existent in the literature. We propose two novel stereo vision-based techniques to this end—a marker-based technique that determines a Lagrangian description for the construction of a Möbius strip, and a structured light illumination technique that furnishes an Eulerian description of its shape. Our measurements enable a critical evaluation of the predictive capabilities of mechanical theories proposed to model Möbius strips. We experimentally validate, seemingly for the first time, the developable strip and the Cosserat plate theories for predicting shapes of Möbius strips. Equally significantly, we confirm unambiguous deficiencies in modelling Möbius strips as Kirchhoff rods with slender cross-sections. The experimental techniques proposed and the Cosserat plate model promise to be useful tools for investigating a general class of problems in ribbon mechanics.

1. Introduction

At over 150 years old, the Möbius strip continues to amaze and inspire [1]. Its profundity is matched only by the simplicity of its construction. To make a Möbius strip, join the ends of a rectangular strip after twisting one of the ends by half a turn. Quite literally, the twist adds magic [2]. It endows the strip with its

THE ROYAL SOCIETY PUBLISHING

characteristic shape and its distinctive one-sided nature. In many ways, the Möbius strip serves as a playground to explore the influence of geometry and topology. Such investigations are no longer limited to abstract mathematics but extend to many science and engineering disciplines. The one-sided nature of the strip has been gainfully exploited in several engineering applications at various length scales, from designing propellers and conveyor belts [3] to fabricating graphene nanoribbons [4], studying DNA structures and biomembranes [5], in synthesizing complex molecules and crystal structures [6], in exploring novel properties of carbon nanostructures [7], probing the mechanics of crumpling paper [8] and even designing new materials [9].

Our study of Möbius strips in this article is motivated by a broader goal of addressing challenges in experimental techniques and modelling approaches in the emerging field of ribbon mechanics [10]. Ribbons are slender elastic structures endowed with three distinct length scales. In the context of a Möbius strip, these dimensions are the length ℓ, the width w, and the thickness t, which are ordered such that $\ell \gg w \gg t$. Recurring themes in the mechanics of ribbon-like structures, such as the contrast between moduli for bending about the principal axes of the cross-section, (near) inextensibility of the mid surface, localization of deformation in the form of creases/vertices, and the interplay between twisting and bending modes of deformation, are all observed in Möbius strips as well [11,12].

Our primary contribution in this article is a novel application of stereo vision techniques to experimentally measure shapes and displacement fields for free-standing Möbius strips. Our measurements, which appear to the be the first of their kind in the literature, represent more than a routine exercise. For a model that serves as a prototypical example in all the STEM fields, experimental studies to quantitatively determine its three-dimensional shape/deformation have remained elusive. To this end, we propose a structured light imaging technique to accurately digitize the shape of a Möbius strip and a marker-based technique to sample the displacement field accompanying its construction. These measurements furnish Eulerian and Lagrangian descriptions for the strip, respectively. Both classes of measurements can be reproduced using a pair of digital cameras, a digital light projector and some proficiency in using open-source computer vision libraries [13]. We expect both techniques to find wider application in digitizing and visualizing deformations of slender elastic structures.

Our experimental measurements also provide an opportune setting to examine the (in)accuracies of mechanical models for predicting shapes and deformations of Möbius strips. Owing to their physical appearance, Möbius strips may be considered either as rods with highly anisotropic cross-sections or as narrow plates. This dichotomy parallels the development of rod- and plate-based models to determine equilibrium shapes of free-standing strips. Among the earliest works on the topic considers minimizing the bending energy of a Kirchhoff plate [14,15]. On the other hand, the strip has also been modelled as a Kirchhoff rod [16] based on the intuitive idea that a rectangular strip can be considered a rod with a slender cross-section. It is generally well recognized that rod and plate models presume drastically different kinematics, and that the latter are better suited for describing deformations of ribbon structures having $w \gg t$ [12,17]. Our investigation here conclusively adds the canonical case of a Möbius strip to the growing list of examples that help distinguish models for slender rods from those for narrow plates.

Specifically, we compare predictions for shapes of Möbius strips modelled as Kirchhoff rods, as developable strips and as Cosserat plates, with experimental measurements. The former pair of one-dimensional theories have been previously investigated in the literature [16,18,19]. However, predictions of neither model appear to have been scrutinized with experimental measurements. Our investigation unambiguously confirms inaccuracies in the number of frame-switching points predicted by the rod theory [18,20] as well as in the dependence of the predicted solution on the width (equivalently the aspect ratio ℓ/w). On the other hand, the measurements fully validate the developable strip model for modelling Möbius strips. As predicted by the simulations in [18], the measurements also confirm the existence of nearly flat triangular facets bounded by sharp creases and localized concentrations (divergences) of the energy density in the strip [11].

Computing predictions of the developable strip model for general ribbon structures, however, remains a challenge [19,21,22]. A fundamental difficulty stems from the choice of parametrization

for the solution surface—the Frenet frame used in the parametrization is ill defined at points where the curvature of the centreline vanishes. The existence and distribution of such points are not known *a priori* and may even change with the applied loading. An added source of difficulty stems from the model's dependence on curvatures and torsions, i.e. on high-order derivatives of the centreline coordinates. Evidently, simulation techniques for ribbon structures based on well-known structural mechanics models using numerical algorithms whose implementations are readily available in simulation codes will be invaluable. This consideration motivates us to examine the more general Cosserat plate theory for modelling Möbius strips. We find that its predictions agree well with the developable strip model, as well as with experimental measurements. Furthermore, the simulations confirm that the theory seamlessly accommodates near inextensibility of the mid surface in bending-dominated deformations. These observations complement the recent findings on the theory's efficacy for modelling annulus-shaped ribbons reported in [12].

The remainder of the article is organized as follows. We provide a concise description of triangulation using a stereo vision arrangement in §2. We propose a marker-based technique to sample displacement fields in constructing Möbius strips in §3 and a structured light imaging technique to measure Möbius strip shapes in §4. We record a few observations based on our measurements of Möbius strips using these techniques in §5. We devote §6 to contrasting experimental measurements with predictions of mechanical models and conclude with a few remarks in §7.

2. Stereo vision in a nutshell

How can we measure the shape of a Möbius strip? Contact-based measurements using probes, for example, are unsuitable because of the compliance of the structure. We resort to optical techniques instead. In principle, photographs of a physical model can be analysed or compared with theoretical predictions [16,23]. Setting aside the challenges in such an exercise (e.g. due to occlusions caused by the strip's shape), the idea is not entirely satisfactory because it only yields projections of the strip on specific planes rather than the actual three-dimensional shape. Instead, we explore the possibility of digitizing the shape of a strip using stereo vision techniques. Hence, we will photograph a Möbius strip from multiple vantage points using a pair of digital cameras and reconstruct its three-dimensional surface using computer vision algorithms. In the interest of keeping our discussions self-contained, we provide a brief description of triangulation in stereo vision in this section.

To fix ideas, we consider the problem of determining the spatial location of a point P given its images as digital photographs. To this end, we describe a simple geometric model for image formation before proceeding to discuss the idea of triangulating the location of P. The ensuing discussions are not intended to review the rich literature on this topic. We refer to [24,25] for details and insights on the general problem of machine vision. Our primary goal here is to facilitate accurate descriptions of the measurement techniques discussed in §§3 and 4.

(a) Image formation

We model a well-focused imaging system as an idealized pinhole camera. Let P have coordinates $\mathbf{X} = (X, Y, Z)$ in a world coordinate system. Let its image be registered at the pixel $\mathbf{x} = (x, y)$ on a digital camera's sensor. The pinhole camera model relates the two as

$$\lambda \underbrace{\begin{bmatrix} x \\ y \\ 1 \end{bmatrix}}_{\bar{\mathbf{x}}} = \underbrace{\begin{bmatrix} s_x & 0 & O_x \\ 0 & s_y & O_Y \\ 0 & 0 & 1 \end{bmatrix}}_{\mathbf{S}} \underbrace{\begin{bmatrix} f & 0 & 0 \\ 0 & f & 0 \\ 0 & 0 & 1 \end{bmatrix}}_{\mathbf{K}_f} \underbrace{\begin{bmatrix} 1 & 0 & 0 & 0 \\ 0 & 1 & 0 & 0 \\ 0 & 0 & 1 & 0 \end{bmatrix}}_{\Pi_0} \underbrace{\begin{bmatrix} \mathbf{R}_{3\times 3} & \mathbf{T}_{1\times 3} \\ 0 & 1 \end{bmatrix}}_{\mathbf{M}} \underbrace{\begin{bmatrix} X \\ Y \\ Z \\ 1 \end{bmatrix}}_{\bar{\mathbf{X}}}, \tag{2.1}$$

or more succinctly, as $\lambda\bar{\mathbf{x}} = \mathbf{S}\mathbf{K}_f\Pi_0\mathbf{M}\bar{\mathbf{X}}$, where $\bar{\mathbf{x}}$ and $\bar{\mathbf{X}}$ denote the homogeneous representations of $\mathbf{x}$ and $\mathbf{X}$, respectively. Equation (2.1) can be interpreted as a sequence of transformations. First, the rigid body transformation $\mathbf{M}$, consisting of a rotation $\mathbf{R}$ and translation $\mathbf{T}$, changes coordinates from the world system to a camera system with its origin at the optical centre and whose z-axis coincides with the optical axis. Next, the canonical perspective projection Π_0 registers P's image on the sensor of a pinhole camera with unit focal length. The product $\Pi = \mathbf{K}_f\Pi_0$ corrects the focal length to f. The point $\mathbf{K}_f\Pi_0\mathbf{M}\bar{\mathbf{X}}$ hence represents the homogeneous coordinates of P's image on the sensor in the camera's coordinate system. The final transformation $\mathbf{S}$ maps these to pixel coordinates using suitable scale factors (s_x, s_y) and a translation (O_x, O_y). The product $\mathbf{K} = \mathbf{S}\mathbf{K}_f$, called the camera matrix, encapsulates all parameters intrinsic to the camera. The set of extrinsic parameters that determine the camera's pose relative to the world coordinate systems is represented by the matrix $\mathbf{M}$. Both $\mathbf{K}$ and $\mathbf{M}$ are identifiable using routine camera calibration procedures [13].

The scale factor λ appearing in equation (2.1) precisely reveals the information lost during image formation, namely, the depth of P along the optical axis. Notice that with $\bar{\mathbf{y}} = \mathbf{K}^{-1}\bar{\mathbf{x}}$ and $\mathbf{Y} = \mathbf{R}\mathbf{X} + \mathbf{T}$, we have

$$\lambda\bar{\mathbf{x}} = \mathbf{S}\mathbf{K}_f\Pi_0\mathbf{M}\bar{\mathbf{X}} \Rightarrow \lambda\bar{\mathbf{y}} = \Pi_0\bar{\mathbf{Y}} \Rightarrow \lambda\bar{\mathbf{y}} = \mathbf{Y}. \tag{2.2}$$

In registering the image of $\mathbf{Y}$ at $\mathbf{y}$, equation (2.2) effectively reduces the imaging system to a canonical pinhole camera with unit focal length. Equation (2.2) also shows that loss of depth during image formation is entirely attributable to the perspective projection $\Pi_0 : \mathbb{R}^4 \to \mathbb{R}^3$. For this reason, a photograph does not help distinguish a Möbius strip from another that is twice as large and is placed twice as far away from the camera.

In summary, equation (2.2) shows that since the depth λ is unknown, it is impossible to determine $\mathbf{Y}$ (equivalently $\mathbf{X}$) using only the pixel coordinates $\mathbf{y}$ (equivalently $\mathbf{x}$), i.e. the relationship $\mathbf{Y} \mapsto \mathbf{y}$ is not invertible. To locate P, it is necessary to image it from at least one more vantage point, which leads us to the idea of triangulation.

(b) Triangulation

As depicted in figure 1, we now assume that P is imaged using a pair of cameras and denote the corresponding realizations of equation (2.2) by $\lambda_1\bar{\mathbf{y}}_1 = \mathbf{Y}_1$ and $\lambda_2\bar{\mathbf{y}}_2 = \mathbf{Y}_2$, respectively, with the subscripts 1 and 2 referring to the camera labels. The depths λ_1 and λ_2 are both unknown. The possibility of determining them emerges from the observation that the pixel locations $\mathbf{y}_{1,2}$ both represent images of the same point P. Since $\mathbf{Y}_1$ and $\mathbf{Y}_2$ represent coordinate transformations of $\mathbf{X}$ to the intrinsic systems of each camera, it follows that $\mathbf{Y}_2 = \mathbf{R}\mathbf{Y}_1 + \mathbf{T}$, where the rotation $\mathbf{R}$ and translation $\mathbf{T}$ constitute the rigid body motion $\mathbf{M}_2^{-1}\mathbf{M}_1$. Then, we have

$$\lambda_2\bar{\mathbf{y}}_2 = \lambda_1\mathbf{R}\bar{\mathbf{y}}_1 + \mathbf{T} \Rightarrow \lambda_1\left(\bar{\mathbf{y}}_2 \times \mathbf{R}\bar{\mathbf{y}}_1\right) = -\bar{\mathbf{y}}_2 \times \mathbf{T} \;\Rightarrow\; \lambda_1 = \frac{\|\bar{\mathbf{y}}_2 \times \mathbf{T}\|}{\|\bar{\mathbf{y}}_2 \times \mathbf{R}\bar{\mathbf{y}}_1\|}, \tag{2.3}$$

from where the desired location $\mathbf{X}$ of P follows as $\bar{\mathbf{X}} = \lambda_1\mathbf{M}_1^{-1}\bar{\mathbf{y}}_1$. Notice that equation (2.3) represents an overdetermined system of equations for the pair of depths λ_1 and λ_2. In fact, the constraint $\lambda_2\bar{\mathbf{y}}_2 = \lambda_1\mathbf{R}\bar{\mathbf{y}}_1 + \mathbf{T}$ on the pixel locations $\mathbf{y}_1$ and $\mathbf{y}_2$ has a useful geometric interpretation:

$$\lambda_2\bar{\mathbf{y}}_2 = \lambda_1\mathbf{R}\bar{\mathbf{y}}_1 + \mathbf{T} \Rightarrow \lambda_2(\mathbf{T} \times \bar{\mathbf{y}}_2) = \lambda_1(\mathbf{T} \times \mathbf{R}\bar{\mathbf{y}}_1) \Rightarrow \bar{\mathbf{y}}_2 \cdot (\mathbf{T} \times \mathbf{R}\bar{\mathbf{y}}_1) = 0 \Rightarrow \mathbf{Y}_2 \cdot (\mathbf{T} \times \mathbf{R}\mathbf{Y}_1) = 0,$$

thus revealing the coplanarity condition illustrated in figure 1. We may therefore interpret the depth calculation in equation (2.3) as a problem of determining the intersection of a pair of rays emanating from the two cameras' optical centres and passing through the image points $\mathbf{y}_1$ and $\mathbf{y}_2$. Such an interpretation justifies the nomenclature of *triangulating* the location of P.

Implicit in the triangulation of P in equation (2.3) is the assumption that it is possible to identify a pixel $\mathbf{y}_1$ (equivalently $\mathbf{x}_1$) in the image from the first camera, and a *corresponding* pixel $\mathbf{y}_2$ (equivalently $\mathbf{x}_2$) in the image from the second, as pixels that represent the same point P. Let us denote the correspondence between $\mathbf{y}_1$ and $\mathbf{y}_2$ by $\mathbf{y}_1 \equiv \mathbf{y}_2$. In practice, this correspondence

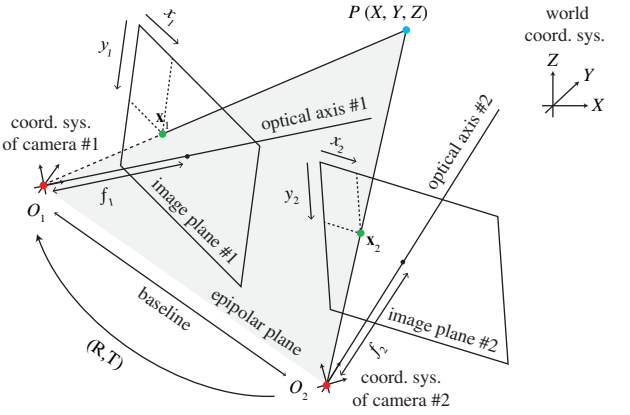

Figure 1. An illustration explaining the triangulation of a point P using a stereo vision arrangement. The optical centres $O_{1,2}$, the image pixels $\mathbf{x}_{1,2}$ and the point of interest P are guaranteed to be coplanar, i.e. to lie on the epipolar plane shown in grey. The three-dimensional location of P is determined as the point of intersection of the rays $O_1\mathbf{x}_1$ and $O_2\mathbf{x}_2$. (Online version in colour.)

problem can be resolved in many ways—by identifying special geometric features in the scene (e.g. corners or edges), matching colours or statistically correlating textures as done in digital image correlation techniques [26]. The techniques described in §§3 and 4 devise special strategies to address the correspondence problem with the specific goal of sampling shapes and displacement fields of Möbius strips.

3. Sampling deformation mappings with fiduciary markers

To sample the deformation mapping for the construction of a Möbius strip, we label its surface with special markers. These markers, which are either pasted or printed on the strip, serve dual purposes. First, tracking marker locations facilitates a Lagrangian description of the construction of the strip. Second, markers help establish pixel correspondences required for triangulation, as discussed above.

(a) ArUco markers

From a variety of strategies for designing markers [27,28], we adopt the fiducial *ArUco* marker system [29]. As depicted in figure 2, markers in this system are square-shaped matrices with binary-encoded bits. Each marker is an $n \times n$ matrix of ones (white) and zeros (black), thus yielding a system with $2^{n\times n}$ markers. However, it is necessary to account for the realistic possibility of errors in bit classification in experimental images, resulting from noise, ambient lighting, shadows and occlusions. This, in turn, is critical for ensuring fault-tolerant marker identification. For this reason, the marker generation system in [29] creates smaller dictionaries by identifying markers that are well spaced in a certain metric. We adopt a 1000-word dictionary of 4×4-bit markers in our experiments.

Figure 2 depicts a stereo arrangement for imaging a Möbius strip. The strip is labelled using ArUco markers, no two of which are identical. Detecting a marker in a camera image yields the pixel coordinates of its four corners. If a marker is detected in both cameras' images, then its location on the strip is reconstructed using equation (2.3). More specifically, let $\mathcal{M}^1$ and $\mathcal{M}^2$ denote the sets of markers detected in the images of cameras 1 and 2, respectively. For $m \in \mathcal{M}^1 \cap \mathcal{M}^2$, let $\{\mathbf{p}_i^{m,1}\}_{i=1}^4$ and $\{\mathbf{p}_i^{m,2}\}_{i=1}^4$ denote the pixel coordinates of the four corners of marker m in the two camera images. Evidently, $\mathbf{p}_i^{m,1} \equiv \mathbf{p}_i^{m,2}$ for each $m \in \mathcal{M}^1 \cap \mathcal{M}^2$ and $i = 1, \ldots, 4$. Thus, triangulating corresponding corner pairs $\mathbf{p}_i^{m,1}$ and $\mathbf{p}_i^{m,2}$ for each $i = 1, \ldots, 4$ using equation (2.3) yields the spatial locations of each corner of m. Figure 3*a* shows images from a representative experiment performed using the set-up in figure 2. To aid in visualization, each marker is assigned a unique colour.

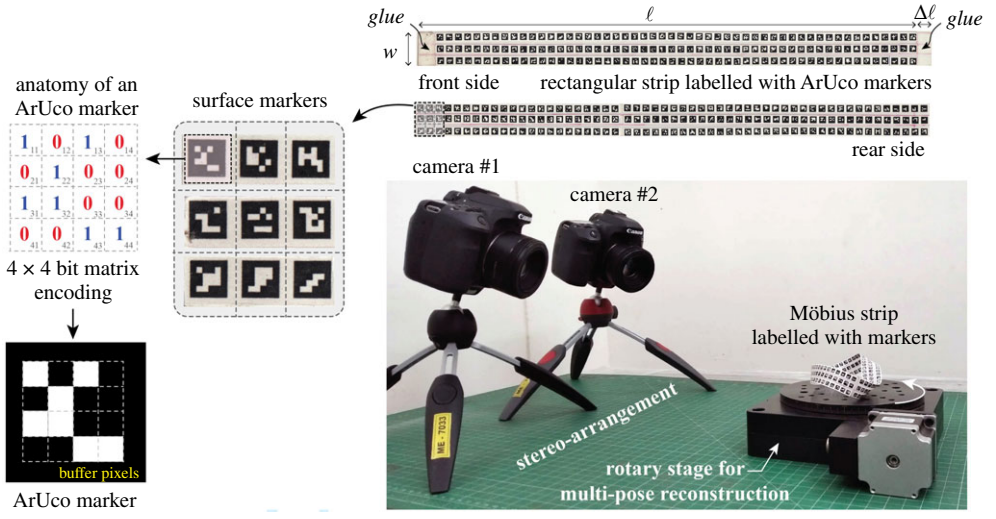

Figure 2. Experimental set-up to sample the deformation mapping of a Möbius strip. Both sides of a rectangular polymeric strip are painted with a non-repeating set of ArUco markers. These markers serve to track material points on the strip and to deduce pixel correspondences. Each marker represents a 4 × 4-bit codeword which can be robustly detected in camera images. (Online version in colour.)

Hence, markers with identical colours appearing in both camera images belong to the set $\mathcal{M}^1 \cap \mathcal{M}^2$, and their corner pixel locations in the two images correspond. The figure also shows the reconstructed set of markers in $\mathcal{M}^1 \cap \mathcal{M}^2$. Denoting the locations of the corners of marker m in the reference configuration by $\{\mathbf{Q}_i^m\}_i$ and their triangulated locations in the deformed configuration by $\{\mathbf{P}_i^m\}_i$, we conclude that marker $m \in \mathcal{M}^1 \cap \mathcal{M}^2$ samples the deformation mapping $\boldsymbol{\varphi}$ and the displacement field $\mathbf{u}$ as

$$\boldsymbol{\varphi}(\mathbf{Q}_i^m) = \mathbf{P}_i^m \quad \text{and} \quad \mathbf{u}(\mathbf{Q}_i^m) = \mathbf{P}_i^m - \mathbf{Q}_i^m. \tag{3.1}$$

(b) Incremental reconstruction

A few practical difficulties arise in realizing the procedure described by equation (3.1). Owing to a Möbius strip's three-dimensional shape, only a small subset of markers on the strip's surface fall within the cameras' fields of view. The detection algorithm may also fail to identify some among them, due to the limited depth of focus, for instance, and especially with markers labelling regions where the strip has large curvatures. In fact, due to the curvilinear shape of the strip, markers are required to be sufficiently small in size for them to be robustly identified by the detection algorithm. Using small markers, in turn, has a cascading set of implications—it requires narrowing the cameras' fields of view, precludes the possibility of using markers with high levels of detail (i.e. a larger number of encoding bits n), and increases the number of markers required to label the strip.

In summary, $\mathcal{M}^1 \cap \mathcal{M}^2$ generally contains only a small fraction of the set of markers used to label the strip. Consequently, it is only possible to sample the deformation/displacement field over a small subset of the strip with a given camera arrangement. For instance, only 75 of the total 321 markers are reconstructed in the stereo arrangement used in figure 3*a*. Therefore, it is necessary to reconstruct marker locations following equations (2.3) and (3.1) incrementally, by altering the relative positioning of the cameras and the strip. In our experiments, it is more convenient to place the strip on a rotary stage than to reposition the cameras. As shown in figure 3*b*, we rotate the stage in 60° increments and compute partial samplings of the deformation mapping at each instance. Finally, we merge all measurement instances to a common coordinate system using a registration procedure. Thus, given the triangulated marker corner locations

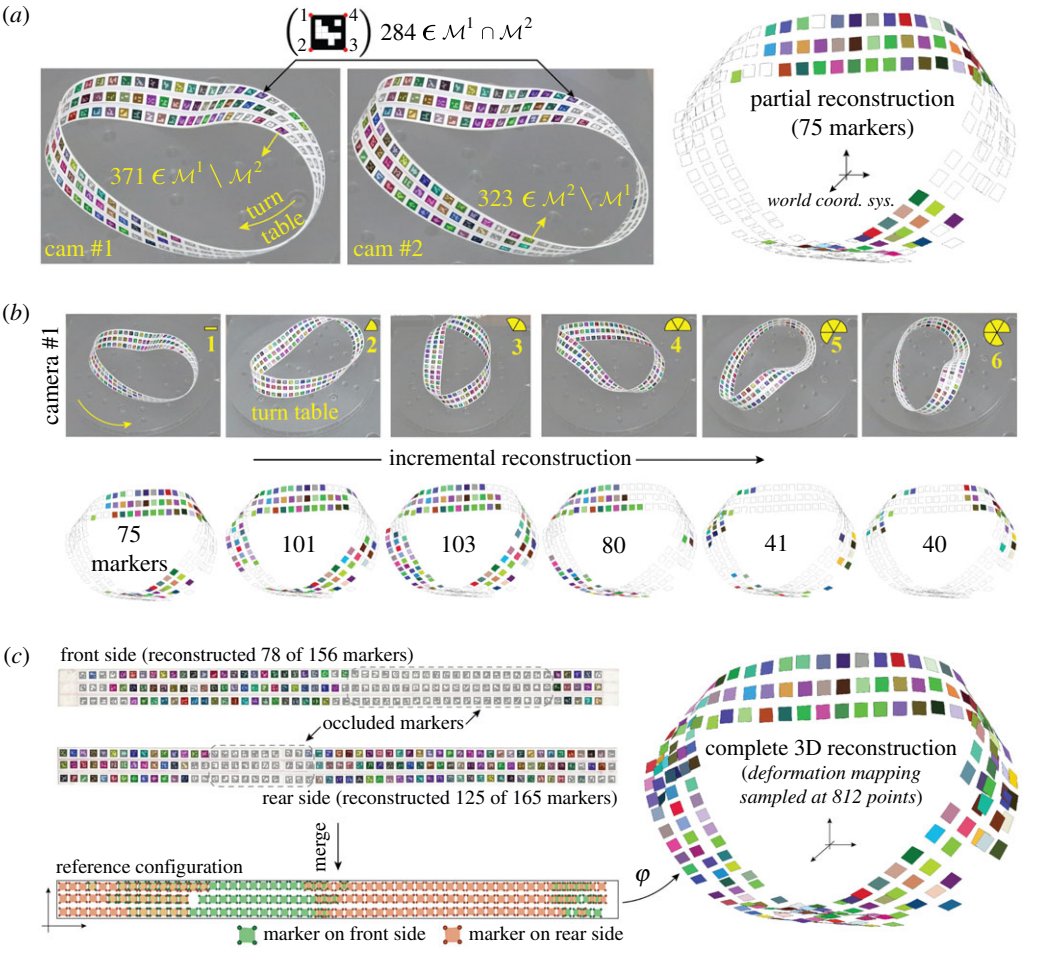

Figure 3. Images (*a*) and (*b*) show partial and incremental reconstructions of surface markers using the set-up in figure 2. The complete reconstruction in (*c*) yields the desired sampling of the deformation mapping defining the construction of the strip. (*a*) The images on the left highlight ArUco markers on the Möbius strip detected in the two cameras' photographs. Each marker is assigned a unique colour to help visualize the set $\mathcal{M}^1 \cap \mathcal{M}^2$ detected in both cameras' images. Respective corners of each of these markers in the two camera images correspond. The result of reconstructing these corner locations is shown on the right. (*b*) Markers on a Möbius strip are incrementally reconstructed in six steps by rotating the turn table on which the sample is placed. Note that only images from camera 1 are shown here. (*c*) Cumulative result of registering partial reconstructions from (*b*). (Online version in colour.)

$\{\mathbf{P}_i^{m,\alpha}\}_{i,m}, m \in \mathcal{M}_\alpha$ and $\{\mathbf{P}^{m,\beta}\}_{i,m} \in \mathcal{M}_\beta$ from a pair of measurement instances labelled α and β, we compute a rigid body transformation $(\mathbf{R}^{\alpha\beta}, \mathbf{T}^{\alpha\beta})$ that maps $\{\mathbf{P}_i^{m,\beta}\}_{i,m}$ to the coordinate system of the instance α. The coordinate transformation is computed by resolving a least-squares minimization problem that registers corners of the common set of markers, namely,

$$\text{Find } (\mathbf{R}^{\alpha\beta}, \mathbf{T}^{\alpha\beta}) \in \mathrm{SO}(3) \times \mathbb{R}^3 \text{ s.t. } \sum_{m \in \mathcal{M}_\alpha \cap \mathcal{M}_\beta} \sum_{i=1}^{4} \|(\mathbf{R}^{\alpha\beta}\mathbf{P}_i^{m,\beta} + \mathbf{T}^{\alpha\beta}) - \mathbf{P}_i^{m,\alpha}\|^2 \to \min. \tag{3.2}$$

Registering measurement instances in a pairwise manner then yields a sampling of the deformation mapping spanning the entire surface of the Möbius strip as shown in figure 3*c*.

Equation (3.2) highlights a third purpose served by the surface markers, namely, pose registration. This is in fact the primary use case for fiduciary markers in augmented reality and robotics applications. Here, we exploit them for a radically different purpose—sampling

deformation mappings of flexible surfaces. The efficacy of such an application relies on the surface remaining (nearly) inextensible so that markers suffer negligible distortions during loading.

4. Sampling three-dimensional shapes using structured light imaging

Owing to the narrow widths of strips, triangulating marker locations, as discussed in §3, only yields a sparse sampling of the shape of a Möbius strip. For instance, the strip appearing in figures 2 and 3 has dimensions $\ell = 30\,\text{cm}$ and $w = 1.9\,\text{cm}$, and the markers used to label the surface have a size of $4\,\text{mm} \times 4\,\text{mm}$. The reconstructed set of 203 markers shown in figure 3*c* yields 812 points sampling the surface, which suffices for analysing coarse geometric features of the surface but does not help examine detailed curvature distributions, for instance. With this rationale, we discuss a structured light imaging technique next that illuminates the strip using distinctive patterns to establish pixel correspondences. The technique yields a dense sampling of the surface, i.e. an Eulerian description for the shape of the strip.

(a) Structured light illumination

The structured light imaging technique we introduce uses binary encoded illumination patterns [30]. As depicted in figure 4, a digital light projector sequentially illuminates a Möbius strip with a hierarchically refined set of patterns, each of which is composed of alternating black and white stripes oriented along the axes of a Cartesian coordinate system. As we explain next, these illumination patterns, which are a defining feature of the technique, serve to encode pixels in cameras imaging the scene. These encodings help establish correspondences between pairs of pixels of cameras in a stereo arrangement, so that corresponding pixel pairs can be triangulated using equation (2.3).

To proceed, it is necessary to introduce some notation. Let images $\{U_i\}_{i=1}^n$ denote the sequence of illumination patterns consisting of alternating black and white stripes oriented along the horizontal direction. With the Möbius strip illuminated using pattern U_i, let I_i^1 and I_i^2 denote the images recorded by the first and second camera, respectively. Similarly, denote the illumination patterns consisting of vertically oriented stripes by $\{V_i\}_{i=1}^n$ and the corresponding camera images by J_i^1 and J_i^2. Without loss of generality, we assume the illumination patterns to be indexed in increasing order of stripe refinement. We also assume camera images to be monochromatic, with intensity values set to 1 at white pixels and 0 at black ones. In the following discussions, we refer to the intensity at pixel (p, q) in an image I by $I(p, q)$.

(b) Encoded correspondences

The sets of camera images $\{I_i^1\}_i \cup \{J_i^1\}_i$ and $\{I_i^2\}_i \cup \{J_i^2\}_i$ all record the same scene with the Möbius strip remaining unperturbed, but under different illuminations. The projected illuminations serve to partition the strip spatially, with each partition encoded by the locally incident sequence of illuminations. In turn, pixel sets of the cameras imaging these regions are partitioned into encoded subsets.

More specifically, define an n-bit codeword $(\mathtt{u}_\alpha, \mathtt{v}_\alpha)$ for the pixel (p, q) in camera α for $\alpha \in \{1, 2\}$, as

$$\mathtt{u}_\alpha(p,q) = (I_1^\alpha(p,q), I_2^\alpha(p,q), \ldots, I_n^\alpha(p,q)) \quad \text{and} \quad \mathtt{v}_\alpha(p,q) = (J_1^\alpha(p,q), J_2^\alpha(p,q), \ldots, J_n^\alpha(p,q)). \tag{4.1}$$

Hence, the codeword $(\mathtt{u}_\alpha(p,q), \mathtt{v}_\alpha(p,q))$ lists the sequence of illuminations recorded at the pixel (p, q) in camera α, with coarser patterns contributing to more significant bits. Equation (4.1) defines an equivalence relation $\sim$ between pixels. Given pixels (p, q) and (p', q') in camera α, we say

$$(p,q) \sim (p',q') \quad \text{if and only if } (\mathtt{u}_\alpha(p,q), \mathtt{v}_\alpha(p,q)) = (\mathtt{u}_\alpha(p',q'), \mathtt{v}_\alpha(p',q')). \tag{4.2}$$

We refer to the equivalence class of pixels determined by the relation $\sim$ as *pixel blocks* and denote the pixel block of camera α with codeword $(\mathtt{u}, \mathtt{v})$ by $\mathrm{B}_\alpha(\mathtt{u}, \mathtt{v})$. Figure 5*a* illustrates such a partitioning

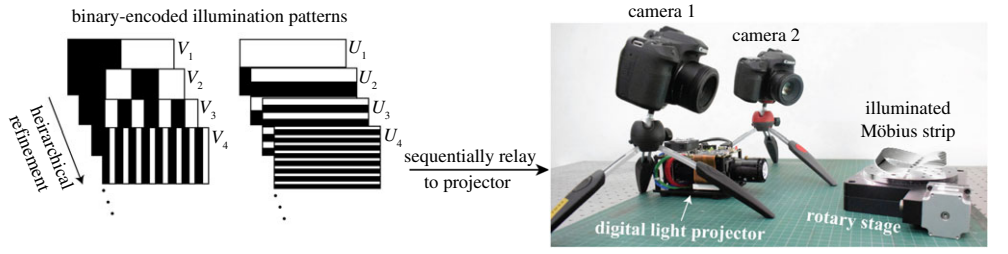

Figure 4. The set-up for sampling the shape of a Möbius strip using structured light illumination patterns consists of a pair of cameras in stereo arrangement and a digital light projector. The latter illuminates the strip with a sequence of binary-encoded light patterns to establish correspondences between pixels of the two cameras. (Online version in colour.)

of pixels of camera 1 into blocks. By recording the same sequence of illuminations, it follows that a pair of pixel blocks B_1 in camera 1 and B_2 in camera 2 correspond if and only if they share the same codeword. In this way, we arrive at a notion of 'block-wise' correspondence between pixels in the two cameras:

$$B_1(u, v) \equiv B_2(u', v') \quad \text{if and only if } (u, v) = (u', v'). \tag{4.3}$$

Figure 5*b* highlights such correspondences by depicting pairs of identically encoded blocks in the same colour.

For triangulation using equation (2.3), equation (4.3) does not suffice because each block generally contains many pixels. The specific numbers depend on the resolutions of the cameras and the projector, the number of illumination patterns used, on geometric features of the strip, and the placement of the cameras. While it is possible to deduce more refined correspondences starting from equation (4.3), we adopt a simpler alternative here by resorting to the ansatz that the averages of pixels in corresponding blocks themselves correspond, i.e. that

$$\langle B_1(u, v)\rangle \equiv \langle B_2(u, v)\rangle \text{ for each } (u, v) \text{ s.t. } B_{1,2}(u, v) \neq \emptyset, \quad \text{where } \langle B\rangle \triangleq \frac{1}{\#B} \sum_{(p,q)\in B} (p, q). \tag{4.4}$$

Note that equation (4.4) is only an approximate notion of correspondence since $B_1(u, v) \equiv B_2(u, v)$ does not imply $\langle B_1(u, v)\rangle \equiv \langle B_2(u, v)\rangle$. However, its accuracy improves with increasing n and with higher projector resolution. Unlike equation (4.3), equation (4.4) is directly suited for triangulation using equation (2.3), which yields a three-dimensional reconstruction of the strip as a dense cloud of points. Figure 5*b* shows the sampling of a Möbius strip computed by projecting $n = 8$ illumination patterns.

As was the case in reconstructing marker locations in §3, it is only possible to sample a subset of a Möbius strip for a given placement of the sample relative to the imaging set-up. In particular, only the subset of the strip falling within the fields of view of the two cameras and the projector is reconstructed. Hence, as illustrated in figure 5*c*, it is necessary to incrementally reconstruct subsets of the strip from multiple vantage points and register them to a common coordinate system. It is worth contrasting the density of the point cloud sampling reconstructed in figure 5*c* with the sparse sampling possible with the marker-based technique (figure 4).

5. Some observations

We record a few remarks concerning the techniques discussed in §§3 and 4 and a few observations from measurements of shapes of Möbius strips using them.

(i) *Accuracy.* Figure 6 examines the accuracies of shape measurements using a polypropylene strip having dimensions $\ell = 30$ cm and $w = 1.9$ cm, by comparing the measurements from figures 3 and 5 with a dense sampling of its surface measured using a laser-based scanner

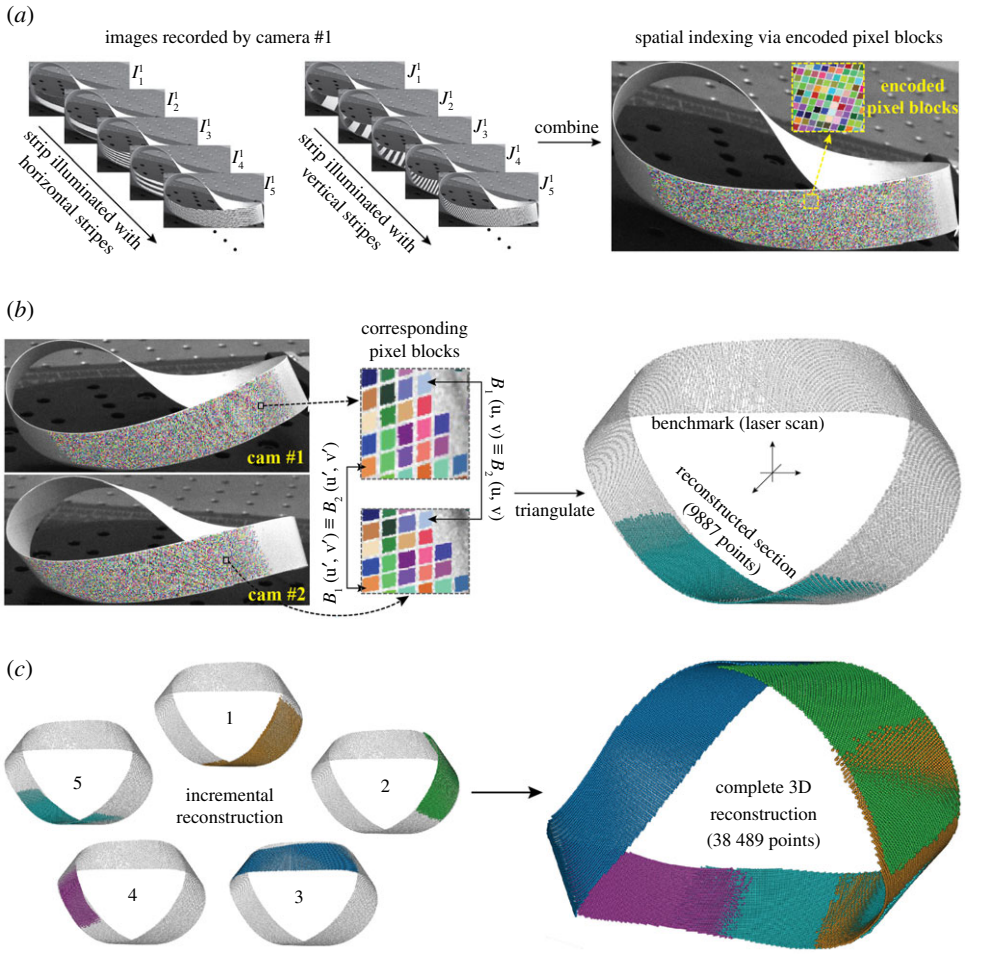

Figure 5. Sampling the shape of a Möbius strip using a structured light illumination technique. (*a*) Sequentially illuminating a strip with structured light patterns spatially partitions camera pixels into encoded blocks. For visualization, such pixel blocks are shown in distinct colours. (*b*) Pixel blocks with identical encodings in both camera images are deemed to correspond. Triangulating corresponding blocks using equation (4.4) yields a point cloud sampling of the strip. (*c*) Incrementally reconstructing a strip from five vantage points. (Online version in colour.)

(Hexagon Romer Arm 7320) that has an accuracy of 80 µm. To quantify the agreement between the measurements shown in the figure, we use the *nearest-neighbour* metric

$$\mathrm{d}(q, \mathcal{P}) \triangleq \min_{p \in \mathcal{P}} \|p - q\| \tag{5.1}$$

that measures the distance of a point q to the point cloud $\mathcal{P}$, where $\|\cdot\|$ is the Euclidean norm in $\mathbb{R}^3$. We denote the benchmark dataset from the laser scan by $\mathcal{P}_{\mathrm{ls}}$, and the measurements determined using ArUco markers and structured light illumination by $\mathcal{P}_{\mathrm{ar}}$ and $\mathcal{P}_{\mathrm{sl}}$, respectively. We find the mean and standard deviation of the distances $\{\mathrm{d}(p, \mathcal{P}_{\mathrm{ls}})\}_{p \in \mathcal{P}_{\mathrm{ar}}}$ to be 44 µm, 27 µm, and of $\{\mathrm{d}(p, \mathcal{P}_{\mathrm{ls}})\}_{p \in \mathcal{P}_{\mathrm{sl}}}$ to be 59 µm, 38 µm. Figure 6 also shows histograms of these distances. These values/plots lead us to conservatively conclude that the measurement errors in the two techniques remain smaller than about 200 µm.

However, it is important to note that the accuracies noted depend on a host of factors. Besides the camera modelling approximations discussed in §2, errors from camera

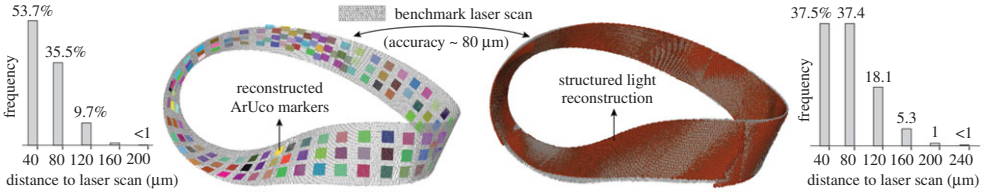

Figure 6. A comparison of the measurements from §§3 and 4 with a benchmark laser scan. (Online version in colour.)

calibration and from registration of partial reconstructions are inevitable. Template matching and corner detection methods underlying ArUco markers' identification, and the ansatz for correspondence assumed in equation (4.4) introduce additional algorithmic sources of error. Besides these, parameters related to the stereo arrangement, such as the baseline distance between the cameras, also influence the measurement accuracy [24,25].

(ii) *Material.* We examine the influence of the material on the shape of a strip in figure 7*a*. The figure compares dense point cloud measurements of shapes of Möbius bands made from 30 cm × 1.9 cm strips cut from a polypropylene sheet (used in figures 3, 5, 6), a radiography film (polyethylene terephthalate base material), and an overhead projector sheet (OHP, polyethylene terephthalate) having nearly identical thicknesses equal to 0.18 mm. We assume the material constitution of each sheet to be nominally isotropic. The figure shows that these datasets, labelled $\mathcal{P}_{\mathrm{pp}}$, $\mathcal{P}_{\mathrm{xray}}$ and $\mathcal{P}_{\mathrm{ohp}}$, respectively, appear to overlap. To quantify the comparison, we compute the mean $\mu(\mathcal{P}_{\mathrm{xray}}, \mathcal{P}_{\mathrm{pp}})$ and standard deviation $\sigma(\mathcal{P}_{\mathrm{xray}}, \mathcal{P}_{\mathrm{pp}})$ of the distances $\{\mathtt{d}(p, \mathcal{P}_{\mathrm{pp}})\}_{p\in\mathcal{P}_{\mathrm{xray}}}$. We find these to be 67 and 54 μm, respectively. Similarly, we find $\mu(\mathcal{P}_{\mathrm{ohp}}, \mathcal{P}_{\mathrm{pp}}) = 36\,\mu\mathrm{m}$ and $\sigma(\mathcal{P}_{\mathrm{ohp}}, \mathcal{P}_{\mathrm{pp}}) = 15\,\mu\mathrm{m}$. These values are comparable to the inter-point spacing ($\approx 44\,\mu\mathrm{m}$) in $\mathcal{P}_{\mathrm{pp}}$ as well as to the accuracies of the measurements noted above, suggesting that the shape of a strip is essentially independent of the material composition. Moreover, we verify that construction of these Möbius strips is fully reversible manner over many trials, thus confirming that the strain in the material does not cause any permanent damage.

(iii) *Width.* Figure 7*b* compares the measured shapes of Möbius strips cut from radiography films having length $\ell = 30$ cm and widths ranging from 1.9 cm to 9.5 cm. The largest width of 9.5 cm is smaller than $\ell/\sqrt{3}$, which is conjectured to be the limiting value to ensure developability [31]. We find that the shapes show small but noticeable differences. In particular, the shape of a strip with a smaller width is *not* simply a subset of a strip with a larger width. We revisit this observation later in §6 when examining the influence of the width on shapes predicted by different mechanical models.

(iv) *Self-weight.* The measurements shown thus far use Möbius strips resting on a turntable (see figures 2 and 4). Strictly speaking, therefore, these strips are not free-standing since the weight of the strip is balanced by contact forces. Figure 7*c* examines the influence of gravity on the shape of a strip (polypropylene, 30 cm × 1.9 cm × 0.18 mm) by measuring its shape when it is rested on a turntable ($\mathcal{P}_H$), and when it is suspended from a support ($\mathcal{P}_V$), as shown in the figure. The locations and relative orientations of gravitational and contact forces acting on the strip are different in the two configurations. Nevertheless, the two measurements agree well with each other—we find $\mu(\mathcal{P}_H, \mathcal{P}_V) = 58\,\mu\mathrm{m}$ and $\sigma(\mathcal{P}_H, \mathcal{P}_V) = 30\,\mu\mathrm{m}$, which are comparable to the measurement accuracy. This observation leads us to infer that Möbius strips made of polymeric materials used in our experiments, all having similar densities and elastic moduli, are sufficiently stiff to resist deformations caused by self-weight. It is important to note, however, that this stiffness is largely geometrically induced and is much smaller in narrower strips. We find that strips with w/ℓ smaller than about 0.035 show notable deformations under self-weight. For this reason, we do not use narrow strips when contrasting experimental measurements with predictions of mechanical models computed without including gravity effects in §6.

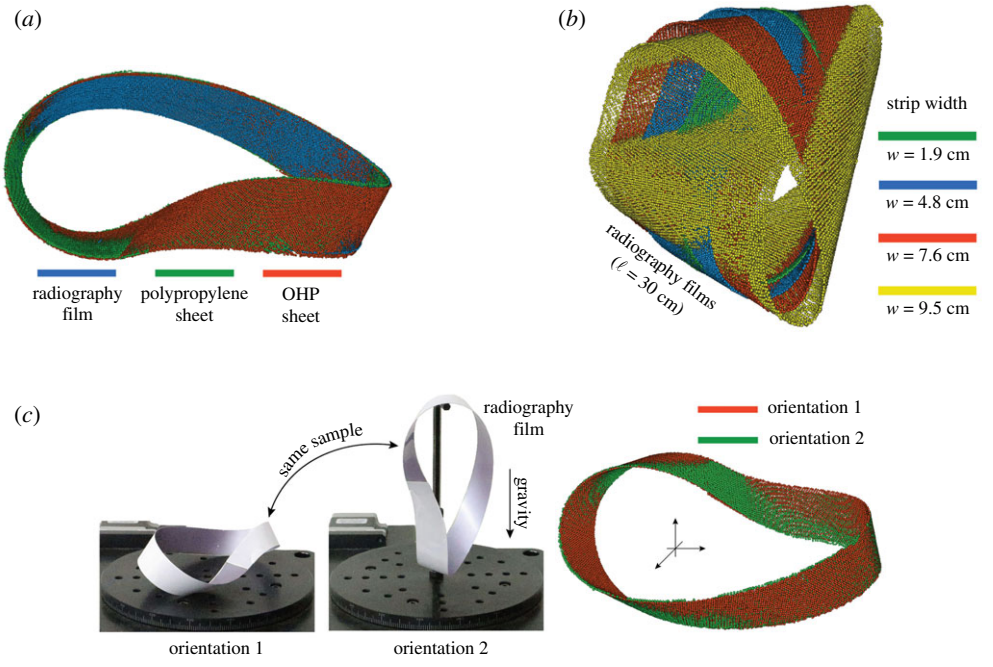

Figure 7. The close agreement between measured shapes of Möbius strips cut from sheets made of three polymeric materials shown in (*a*) suggests that the influence of the material is negligible, provided that strains remain small and the material constitution is isotropic. The image in (*b*) compares the shapes of strips having identical length but different widths. Small differences in the shapes are evident. The images in (*c*) confirm the negligible influence of self-weight on the shape of a Möbius strip by contrasting measurements with two different types of supports. All strips shown have length $\ell = 30$ cm; the strips in (*a*) and (*c*) have width $w = 1.9$ cm. (Online version in colour.)

(v) *Thickness independence.* We expect surfaces of thin Möbius strips to remain developable. To verify that our experiments fall in a bending dominated regime, we construct Möbius bands from polypropylene sheets having dimensions $\ell = 30\,\text{cm}$, $w = 1.9\,\text{cm}$ and thicknesses equal to 100, 180 and 230 μm using the procedure shown in figure 2. The overlap length $\Delta\ell$ is set to 10 mm in each case. We compare dense point cloud measurements $\mathcal{P}_{100}, \mathcal{P}_{180}$ and $\mathcal{P}_{230}$ of their shapes with the measurement $\mathcal{P}_{\text{ref}}$ of a *reference band* whose construction is depicted in figure 8*a*. Specifically, we create the reference band by cutting a rectangular strip with dimensions $2\ell \times w$ from a polypropylene sheet with thickness $t = 180\,\mu\text{m}$ and apply an adhesive over one half of its length. We bend, twist and wind the strip to emulate the construction of a Möbius band from a strip having dimensions $\ell \times w$ but thickness $2t = 360\,\mu\text{m}$. We find that the mean $\mu(\mathcal{P}_t, \mathcal{P}_{\text{ref}})$ and standard deviation $\sigma(\mathcal{P}_t, \mathcal{P}_{\text{ref}})$ for $t = 100, 180$ and $230\,\mu\text{m}$ reported in figure 8*b* are comparable to the measurement accuracies. This leads us to conclude that the four Möbius bands with different thicknesses have nearly indistinguishable shapes, i.e. that band shapes are independent of the thickness over the range of aspect ratios considered.

(vi) *Thickness perturbations.* The last observation we note concerns the influence of local perturbations in the thickness of a strip on its shape. Such perturbations manifest in our experiments in two ways. First, we prepare Möbius bands by gluing the ends over a small but finite overlap region as indicated in figure 2. Consequently, the thickness of the band is doubled over an area measuring $\Delta\ell \times w$. A second source of perturbations arises from pasting markers on the strip, which locally increases the thickness. We examine the (in)significance of these thickness perturbations in figure 8. With the rationale that the reference band in figure 8*a* is devoid of thickness perturbations, we set $\mathcal{P}_{\text{ref}}$ to be the

(*a*)

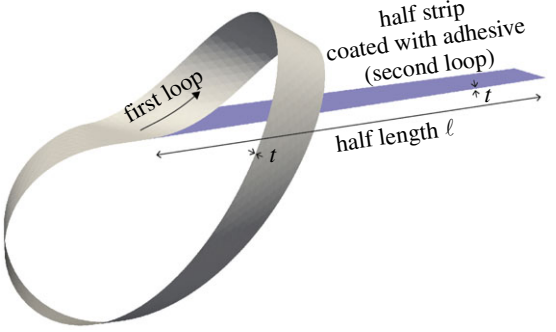

(*b*)

thickness t (μm)	mean (μm)	s.d. (μm)
100	73	52
180	95	53
230	82	62

overlap $\Delta\ell$ (mm)	mean (μm)	s.d. (μm)
5	68	42
10	95	53
15	89	48
20	90	50

(*c*)

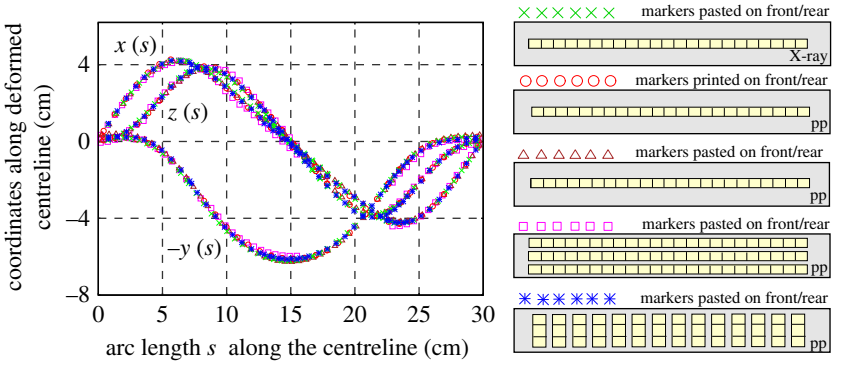

Figure 8. Examining the influence of the thickness and thickness perturbations on the shape of a Möbius strip. The reference 'double-layer' band constructed as shown in (*a*) is free from thickness variations and therefore serves as the benchmark dataset. Table (*b*) confirms that the thickness and the overlap length have negligible influence on the shape, while (*c*) verifies insensitivity to different combinations of strip materials, the number of markers pasted, and marker arrangements. (Online version in colour.)

benchmark dataset against which we compare point cloud measurements from Möbius strips (polypropylene, 30 cm × 1.9 cm × 0.18 mm) having overlap lengths ranging from 5 to 20 mm. The mean and standard deviations computed from these comparisons are reported in figure 8*b*. These values are comparable to the measurement accuracy and are within acceptable bounds for the case $\Delta\ell = 10$ mm used in all our experiments. Finally, figure 8*c* compares the centreline coordinates of strips (polypropylene, 30 cm × 1.9 cm × 0.18 mm) measured in five experiments using different combinations of pasted markers, printed markers, and marker arrangements. The plots confirm that the band's shape is unaffected by markers, and hence that the effects of thickness perturbations in our samples are inconsequential.

6. Model predictions versus measurements

Measurements of shapes and deformation maps of Möbius strips enable us to critically examine the predictive capabilities of mechanical theories proposed to model them. Since details of these models are well documented in the literature, we restrict their discussions to just the aspect relevant to their numerical simulation.

(a) Mechanical models

In the following, the unstressed configuration of the strip coincides with the region $\mathcal{B}_0 = \mathcal{S}_0 \times [-h/2, h/2]$, where $\mathcal{S}_0 = \mathcal{C}_0 \times [-w/2, w/2]$ is the mid surface of the strip and $\mathcal{C}_0 = [0, \ell]$ is the centreline oriented along the $\mathbf{E}_1$ axis in the standard Cartesian basis $\{\mathbf{E}_1, \mathbf{E}_2, \mathbf{E}_3\}$. A Möbius strip is constructed by rotating and twisting the edge $X_1 = \ell$ while holding the edge $X_1 = 0$ fixed (see figure 9). We are interested in predicting the shapes of the deformed mid surface $\mathcal{S}$ and the deformed centreline $\mathcal{C}$.

(i) Möbius strips as Kirchhoff rods

The configuration of a Möbius strip modelled as a Kirchhoff rod is specified by its centreline $\mathbf{r} : [0, \ell] \to \mathbb{R}^3$ that is endowed with an orthonormal triad of directors $\{\mathbf{t}_1, \mathbf{t}_2, \mathbf{t}_3\}$ at each point (see figure 9*a*). In the unstressed configuration, $\mathbf{r}(X_1) = X_1\mathbf{E}_1$ and the director frame coincides with the Cartesian basis The centreline remains inextensible during deformation, i.e. $\|\mathbf{r}'\| = 1$, where $(\cdot)' = \mathrm{d}(\cdot)/\mathrm{d}X_1$. Unshearability of cross-sections orthogonal to the centreline is enforced by the constraint $\mathbf{r}' = \mathbf{t}_1$.

Introducing $\boldsymbol{\omega} : [0, \ell] \to \mathbb{R}^3$ such that $\mathbf{t}_i' = \boldsymbol{\omega} \times \mathbf{t}_i$ with $\boldsymbol{\omega} = \kappa_1\mathbf{t}_1 + \kappa_2\mathbf{t}_2 + \kappa_3\mathbf{t}_3$ identifies κ_1 as the torsional strain measuring twist of the director frame about $\mathbf{t}_1$, and κ_2 and κ_3 to be the strains for bending about the axes $\mathbf{t}_2$ and $\mathbf{t}_3$, respectively. Presuming a linear constitutive relationship between these strain measures and their conjugate moment resultants, the strain energy functional associated with the configuration $(\mathbf{r}, \{\mathbf{t}_i\}_i)$ follows as [32, ch. 5]

$$\Pi^{\mathrm{rod}}[\mathbf{r}, \{\mathbf{t}_i\}_i] = \frac{1}{2}\int_{X_1=0}^{\ell} \left(GJ\kappa_1^2 + EI_2\kappa_2^2 + EI_3\kappa_3^2\right) \mathrm{d}X_1, \tag{6.1}$$

where E and G are the Young and shear moduli, $I_2 = wh^3/12$ and $I_3 = hw^3/12$ are the area moments of inertia of the cross-section $[-w/2, w/2] \times [-h/2, h/2]$ for bending about $\mathbf{t}_2$ and $\mathbf{t}_3$, respectively, and $GJ \approx (G/3)wh^3(1 - 0.63h/w)$ is the torsional stiffness. Moments $\mathbf{m}$ along the centreline are constitutively defined, while contact forces $\mathbf{n}$ are Lagrange multipliers imposing the inextensibility and unshearability constraints. Statements of force and moment balances yield the familiar differential equations $\mathbf{n}' = 0$ and $\mathbf{m}' + \mathbf{t}_1 \times \mathbf{n} = 0$.

To mimic the construction of a Möbius strip, the centreline and the director frame at the end $X_1 = 0$ are constrained by setting $(\mathbf{r}, \mathbf{t}_1, \mathbf{t}_2, \mathbf{t}_3) = (0, \mathbf{E}_1, \mathbf{E}_2, \mathbf{E}_3)$ at $X_1 = 0$. Assuming flip-symmetry of the solution about the $\mathbf{E}_2$ axis [16,19], the centreline is constrained to lie on the $\mathbf{E}_2$ axis and the director $\mathbf{t}_3$ is oriented anti-parallel to $\mathbf{E}_2$ at $X_1 = \ell/2$. Moreover, components of the contact force and moment along the symmetry axis vanish as well. Hence, we set $(\mathbf{r} \cdot \mathbf{E}_1, \mathbf{r} \cdot \mathbf{E}_3, \mathbf{t}_3, \mathbf{n} \cdot \mathbf{E}_2, \mathbf{m} \cdot \mathbf{E}_2) = (0, 0, -\mathbf{E}_2, 0, 0)$ at $X_1 = \ell/2$. In summary, an equilibrium configuration $(\mathbf{r}, \{\mathbf{t}_i\}_i)$ for the Möbius strip predicted by the Kirchhoff rod model is an extremizer of the energy functional Π^{rod} in equation (6.1) satisfying the clamped and flip-symmetry boundary conditions at $X_1 = 0$ and $\ell/2$, respectively.

(ii) Möbius strips as developable surfaces

The point of departure for modelling the construction of a developable Möbius strip is the bending energy of a Kirchhoff plate [33, ch. 24]:

$$\Pi^{\mathrm{kp}}[\mathcal{S}] = \frac{B}{2}\int_{\mathcal{S}} \{(1-\nu)\mathrm{Tr}[\mathbf{K}^2] + \nu\,\mathrm{Tr}^2[\mathbf{K}]\}\,\mathrm{d}\mathcal{S}, \tag{6.2}$$

which presumes a linearly elastic and isotropic material constitution, and where $B = Eh^3/12(1-\nu^2)$ is the bending modulus, ν is Poisson's ratio and $\mathbf{K}$ denotes the curvature tensor of the mid surface $\mathcal{S}$. Developability of $\mathcal{S}$ implies $\det(\mathbf{K}) = 0$, which simplifies equation (6.2) to $\Pi^{\mathrm{kp}}[\mathcal{S}] = (B/2)\int_{\mathcal{S}} \mathrm{Tr}^2[\mathbf{K}]\,\mathrm{d}\mathcal{S}$. Furthermore, the developability constraint inspires a special parametrization for the strip as a ruled surface [23]. Consequently, the configuration $(\mathbf{r}, \eta)$ of the mid surface is defined by its centreline $X_1 \mapsto \mathbf{r}(X_1)$ whose Frenet frame consisting of the

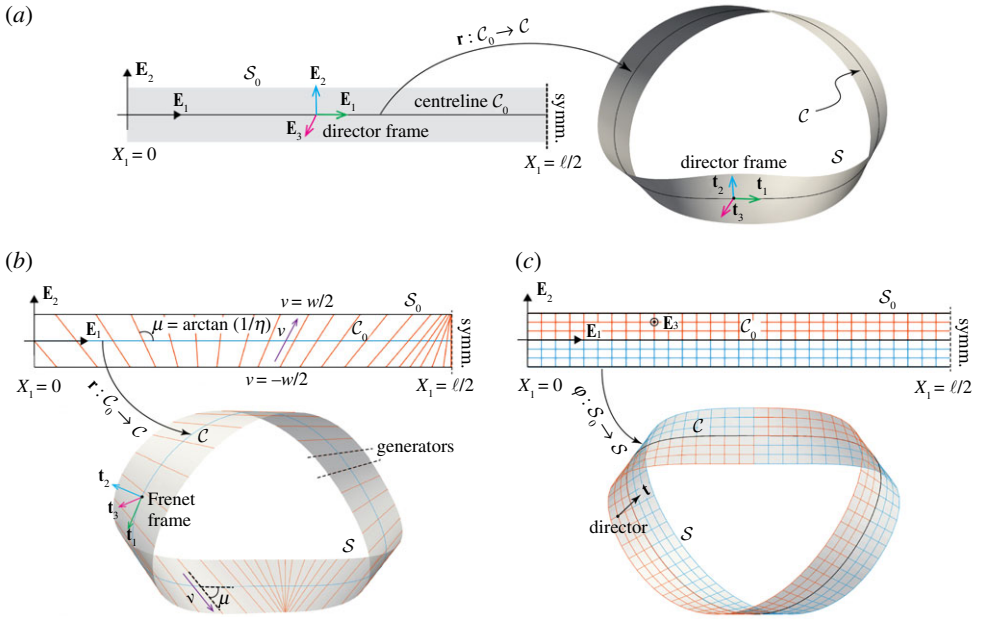

Figure 9. Parametrizations of a Möbius strip modelled as a Kirchhoff rod (*a*), developable strip (*b*) and as a Cosserat plate (*c*). (Online version in colour.)

unit tangent, binormal and normal is denoted by $\{\mathbf{t}_1, \mathbf{t}_2, \mathbf{t}_3\}$, and a field $X_1 \mapsto \eta(X_1) \in \mathbb{R}$ defining inclinations of surfaces generators belonging to tangent planes spanned by $\mathbf{t}_1$ and $\mathbf{t}_2$ (see figure 9*b*). Setting the generator at $\mathbf{r}(X_1)$ as $\mathbf{t}_2(X_1) + \eta(X_1)\,\mathbf{t}_1(X_1)$ and denoting the coordinate along a generator by v, the parametrization of the mid surface follows as $(X_1, v) \mapsto \mathbf{r}(X_1) + v(\mathbf{t}_2(X_1) + \eta(X_1)\,\mathbf{t}_1(X_1))$, where $\mathbf{t}_1(X_1) = \mathbf{r}'(X_1)$. The pullbacks of the Frenet frame and the generators to the unstressed configuration are $\{\mathbf{E}_1, \mathbf{E}_2, \mathbf{E}_3\}$ and $\mathbf{E}_2 + \eta(X_1)\,\mathbf{E}_1$, respectively, thus yielding a parametrization for $\mathcal{S}_0$ as $(X_1, v) \mapsto X_1\mathbf{E}_1 + v(\mathbf{E}_2 + \eta(X_1)\,\mathbf{E}_1)$. In particular, the lateral edges of the rectangular strip along $X_2 = \pm w/2$ coincide with the bounds $v = \pm w/2$ along each generator. Hence, $(X_1, v) \in [0, \ell] \times [-w/2, w/2]$.

The mid surface parametrization together with the observation that $\mathbf{t}_i' = \boldsymbol{\omega} \times \mathbf{t}_i$ for $\boldsymbol{\omega} = -\tau\mathbf{t}_1 - \kappa\mathbf{t}_2$, where κ and τ are the curvature and torsion of the centreline, respectively, reduce Π^{kp} to the one-dimensional Wunderlich functional (see [34, appendix] and [35]):

$$\Pi^{\mathrm{kp}}[\mathcal{S}] = \frac{Bw}{2}\int_{X_1=0}^{\ell} \frac{\kappa^2(1+\eta^2)^2}{\eta' w}\log\left(\frac{2+\eta' w}{2-\eta' w}\right)\mathrm{d}X_1 \equiv \Pi^{\mathrm{ds}}[\mathbf{r}, \eta]. \tag{6.3}$$

In the interest of brevity, we omit stating the equilibrium equations satisfied by extremizers of Π^{ds}, which can be found in [18]. To simulate the construction of a Möbius strip, we impose boundary conditions analogous to the case of the rod model.

(iii) Möbius strips as Cosserat plates

The Wunderlich functional effectively models Möbius strips as Kirchhoff plates in pure bending. The 1-director Cosserat plate model relaxes the mid surface inextensibility and transverse unshearability constraints. The admissible configuration $(\boldsymbol{\varphi}, \mathbf{t})$ of a Möbius strip modelled as a Cosserat plate is specified by its mid surface $\boldsymbol{\varphi} : \mathcal{S}_0 \to \mathbb{R}^3$ and a director field $\mathbf{t} : \mathcal{S}_0 \to \mathbb{S}^2$ having unit norm (see figure 9*c*). The latter is interpreted to denote the inclinations of inextensible material fibres oriented along the thickness in the unstressed state, where $\boldsymbol{\varphi}(X_1, X_2) = X_1\mathbf{E}_1 + X_2\mathbf{E}_2$ and $\mathbf{t} = \mathbf{E}_3$.

Equilibrium configurations are extremizers of the energy functional

$$\Pi^{\mathrm{cp}}[\boldsymbol{\varphi},\mathbf{t}] = \frac{1}{2}\int_{\mathcal{S}_0} \frac{Eh}{(1-\nu^2)}\left(\nu\,\mathrm{Tr}^2[\boldsymbol{\varepsilon}] + (1-\nu)\mathrm{Tr}[\boldsymbol{\varepsilon}^2]\right) + Gh\,(\boldsymbol{\gamma}\cdot\boldsymbol{\gamma}) + B\left(\nu\,\mathrm{Tr}^2[\boldsymbol{\kappa}] + (1-\nu)\mathrm{Tr}[\boldsymbol{\kappa}^2]\right)\mathrm{d}\mathcal{S}_0, \tag{6.4}$$

which consists of contributions from membrane, transverse shear and bending modes of deformation. The corresponding strain measures $\boldsymbol{\varepsilon},\boldsymbol{\gamma}$ and $\boldsymbol{\kappa}$ have components $\varepsilon_{\alpha\beta} = (\boldsymbol{\varphi}_{,\alpha}\cdot\boldsymbol{\varphi}_{,\beta} - \delta_{\alpha\beta})/2$, $\gamma_\alpha = \boldsymbol{\varphi}_{,\alpha}\cdot\mathbf{t}$ and $\kappa_{\alpha\beta} = \boldsymbol{\varphi}_{,\alpha}\cdot\mathbf{t}_{,\beta}$ in the basis dual to the mid surface tangents $\{\boldsymbol{\varphi}_{,1},\boldsymbol{\varphi}_{,2}\}$, where $\alpha,\beta\in\{1,2\}$ and we have used the shorthand $(\cdot)_{,\alpha}$ to denote the partial derivative $\partial(\cdot)/\partial X_\alpha$. Equation (6.4) presumes a linear constitutive relationship between these strains and their conjugate stress resultants. In particular, $Eh/(1-\nu^2)$, Gh and B are the membrane, transverse shear and bending moduli, respectively. Finally, the boundary conditions satisfied by the deformation to replicate the construction of a Möbius strip are given by

$$(\boldsymbol{\varphi},\mathbf{t})\big|_{X_1=0} = (X_2\mathbf{E}_2,\mathbf{E}_3) \quad \text{and} \quad (\boldsymbol{\varphi},\mathbf{t})\big|_{X_1=\ell} = -(X_2\mathbf{E}_2,\mathbf{E}_3). \tag{6.5}$$

Evidently, the Cosserat plate theory relaxes the assumptions of centreline inextensibility and unshearability of cross sections assumed in the Kirchhoff rod and developable strip models. In light of the bending dominated nature of the deformations highlighted by the insensitivity of band shapes to strip thicknesses in figure 8*b*, we do not expect this generality of the theory to be significant for modelling thin Möbius strips. This expectation is confirmed by the numerical simulations shown subsequently. Nevertheless, permitting transverse shear simplifies the choice of coordinates (i.e. degrees of freedom) in the finite-element method by avoiding the need for continuously differentiable basis functions. The large contrast between bending and shear stiffnesses effectively penalizes transverse shear. Notice also that unlike in the one-dimensional models, we do not presume flip-symmetry in equation (6.5). Nevertheless, all our simulations of Möbius strips using the Cosserat plate theory reveal this symmetry.

(b) Models versus measurements

We now proceed to compare model predictions with experimental measurements. Unless mentioned otherwise, we consider the strip used in §§3 and 4 having dimensions $\ell = 30\,\mathrm{cm}$, $w = 1.9\,\mathrm{cm}$ and $t = 0.18\,\mathrm{mm}$ in all the subsequent discussions. In keeping with the conventional choice of examining strips having length 2π [16,18,19], we scale the experimental measurements uniformly by the factor $2\pi/30$ and accordingly set $\ell = 2\pi, w = 0.4$ and $t = 0.00377$ in our simulations to retain the aspect ratios $\ell/w \approx 15.7$ and $w/t \approx 105.6$.

(i) Centreline shapes

Figure 10 shows projections of predicted and measured centreline shapes on orthogonal Cartesian planes. We are grateful to Starostin & van der Heijden [18] for sharing simulation results for the developable strip model, which we have used as-is. To compute the Cosserat plate model's predictions, we use the nonlinear finite-element method discussed in [36] and adopt cubic triangular elements to circumvent issues of numerical locking. The top row of plots in the figure reveals that the two models agree well with each other and with the marker-based experimental measurements.

The second row of plots contrasts the same measurements with the prediction of the Kirchhoff rod model. To examine whether the inextensibility and unshearability constraints presumed in the model contribute to the large deviations observed, the plots additionally show predictions of a generalized Cosserat rod model from [37] and a simulation performed using the commercial software Abaqus (element-type B33). The former permits centreline extension and transverse shear, while the latter permits centreline extension but not shear. We find that the shapes predicted by all three models coincide. Moreover, extensional and shear strains remain negligibly small in

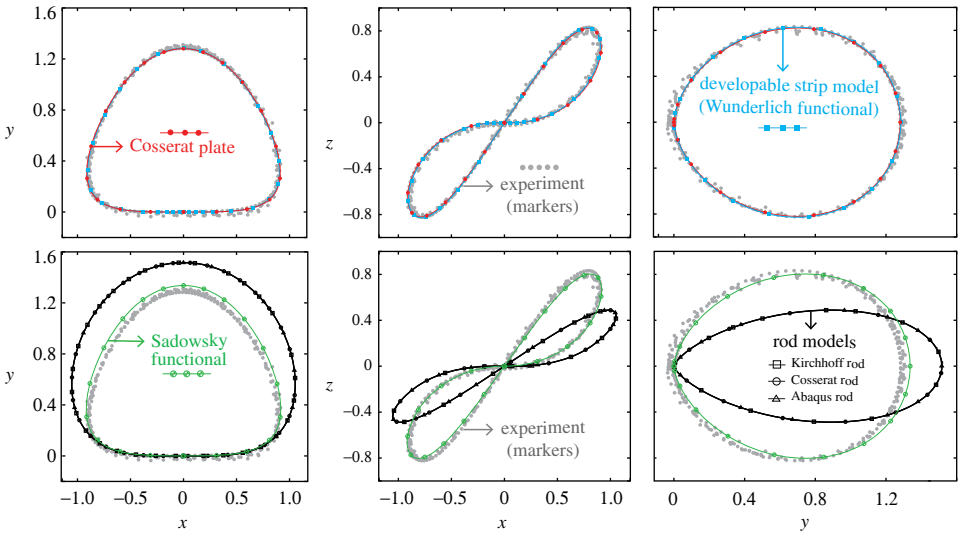

Figure 10. Measured and predicted centreline shapes of a Möbius strip having dimensions $\ell = 2\pi$, $w = 0.4$ and $t = w/105.5$. The top row compares experimental marker-based measurements from figure 8 with predictions of the developable strip and Cosserat plate models. The bottom row similarly compares the predictions of one-dimensional nonlinear rod and Sadowsky models. (Online version in colour.)

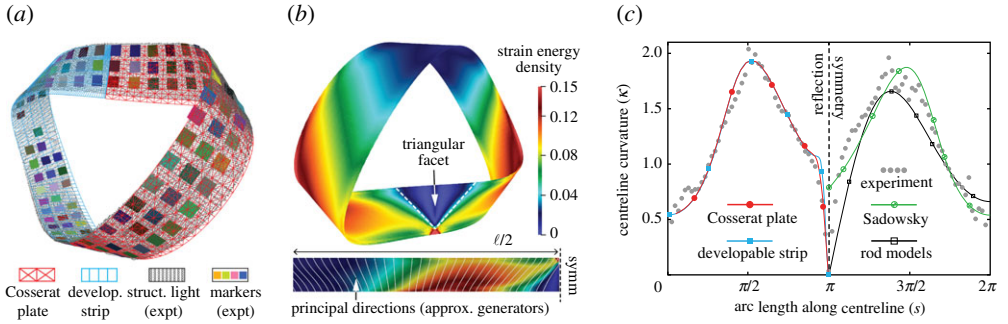

Figure 11. An examination of deformation features in a Möbius strip. Image (*a*) compares predicted and measured strip shapes, complementing the observations on centreline shapes in figure 10. (*b*) Contours of the strain energy density Π^{cp}/B over the reference and deformed configurations predicted by the Cosserat plate model. The plot in (*c*) examines the curvature of the centreline computed from measurements and model predictions. (Online version in colour.)

these simulations even when permitted, thus reaffirming the deformation's bending-dominated nature.

The curve in green shown in the bottom row of plots is an extremizer of the Sadowsky functional [14,15] $\Pi^{\mathrm{sy}} = (Bw/2)\int_0^\ell (\kappa^2+\tau^2)^2/\kappa^2 \, \mathrm{d}X_1$, where κ and τ denote the curvature and torsion of the centreline. The model can be formally derived from equation (6.3) as the width w is made vanishingly small. The Sadowsky model's prediction is notably superior to the rod models. Nevertheless, its qualitative deficiencies become apparent when we examine the prediction of κ in figure 11*c*.

(ii) Deformation features

Figure 11*a* complements the centreline comparisons in figure 10 by examining the predicted and measured shapes of mid surfaces. The developable strip model defines the mid surface as the rectifying developable of the predicted centreline, while the Cosserat plate theory computes the

mid surface explicitly. Figure 11*a* superimposes these with the marker-based and the structured light imaging measurements. We find that all four datasets agree well with each other.

A prominent feature the shape of a Möbius strip is the manifestation of nearly flat triangular regions bounded by creases [38]. Such phenomena are of interest in studying energy localization and are understood to result from coupling between bending and twisting deformation modes [11]. To examine this feature, figure 11*b* shows contours of the strain energy density predicted by the Cosserat plate model over the reference and deformed mid surfaces. The triangular facet is highlighted over the latter. The energy density is negligibly small over the demarcated region, confirming that the facet is in fact nearly flat. The creases bounding the facet appear to meet at a vertex, where the strain energy is localized. Such vertices are points where generators accumulate in the developable strip model [18]. However, the Cosserat plate theory does not invoke any notion of developability and hence makes no references to surface generators. Instead, the bending dominated nature of the deformation ensures negligible metric distortions. To highlight this feature of the Cosserat model's prediction, we compute the eigen decomposition of the second fundamental form of the deformation mapping predicted by it for the mid surface. We find that the Gaussian curvature indeed remains negligibly small. Furthermore, the eigenvectors corresponding to the (approximately) zero eigenvalue plotted over the reference configuration in figure 11*b* closely resemble the distribution of generators observed in the developable strip model see (see [18, fig. 2]).

Figure 11*c* examines the curvatures (κ) of the centreline shapes in figure 8. We note that κ is one of the primary unknowns in the developable strip model, but is not of particular significance in the Cosserat plate model and is computed as a post-processing step. We resort to a spline fit ($R^2 > 0.99$) to determine the curvature distribution from the experimental measurements. The figure reveals that centreline curvatures computed from both models and the measurements agree well. Notice that the curvature vanishes at $s = \pi$ in all three datasets. Indeed, the Frenet frame switches orientation at this point. Nevertheless, the mid surface parametrization remains continuous thanks to the vanishing curvature. This is not the case with the Sadowsky model shown in green, for which $\kappa(\pi) \neq 0$. The figure also helps examine the number of frame-switching points, where both the curvature and torsion of the centreline vanish. It is shown in [20] that the centreline of a developable Möbius strip necessarily has an odd number of such points. Although we have omitted plots showing torsion of the centreline, we note that both the developable strip and Cosserat plate models identify precisely one such point at $s = \pi$. By contrast, the Kirchhoff rod model violates this condition [18].

(iii) Influence of the width

The measurements depicted in figure 7*b* reveal a noticeable influence of the width on a Möbius strip's shape. Both the developable strip and the Cosserat plate models reproduce this dependence accurately. Figure 12*a* quantitatively conveys this agreement by reporting the mean and standard deviations, μ, σ as defined in §5, of a dense set of points sampling the mid surfaces predicted by the Cosserat plate and developable strip models, from the measurements shown in figure 7*b*. By contrast, we find that the Kirchhoff rod model predicts identical centreline shapes for all the four widths considered in figure 12*a*. This observation can be rationalized as follows. At large values of the aspect ratio w/t, the contribution to the strain energy Π^{rod} in equation (6.1) from bending about the stiff axis $\mathbf{t}_3$ becomes negligibly small, i.e. $\int_{X_1=0}^{\ell} EI_3\kappa_3^2 \, \mathrm{d}X_1 \approx 0$. In this regime, J is well approximated by $wh^3/3$. Hence, both $\int_{X_1=0}^{\ell} GJ\kappa_1^2$ and $\int_{X_1=0}^{\ell} EI_2\kappa_2^2$ depend linearly on w, thus rendering Π^{rod}/w independent of the width.

(iv) Energies

Figure 12*b* examines the strain energies of predicted solutions for strips having widths considered in figure 12*a*. The energies are normalized by the bending modulus B of the plate theory. Corroborating the close agreements observed in figures 10 and 11, we find that the energies

(*a*)

width w in cm	developable strip (mean, s.d.) in µm	Cosserat plate (mean, s.d.) in µm
1.90	60, 27	69, 28
4.78	53, 19	54, 22
7.64	68, 39	84, 49
9.55	84, 67	104, 63

(*b*)

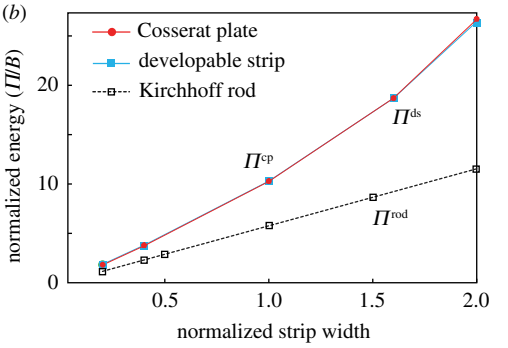

Figure 12. Table (*a*) reports the means and standard deviations (μ and σ as defined in §5) of the predictions by the developable strip and Cosserat plate models from point cloud measurements of 30 cm long strips having different widths. The plot in (*b*) shows normalized strain energies as a function of the normalized width for Möbius strips modelled as a nonlinear rod, developable strip and as a Cosserat plate. (Online version in colour.)

predicted by the developable strip and Cosserat plate models agree well. Inspecting the simulated solutions confirms this to be a consequence of the membrane and shear components of the energy in the Cosserat plate theory being negligibly small. Indeed, examining the non-dimensionalized ratios of membrane and shear moduli to the bending modulus

$$\frac{\ell w \times Eh/(1-\nu^2)}{B} = 12\left(\frac{\ell}{w}\right)\left(\frac{w}{h}\right)^2 \quad \text{and} \quad \frac{\ell w \times Gh}{B} = 6(1-\nu)\left(\frac{\ell}{w}\right)\left(\frac{w}{h}\right)^2,$$

shows that the membrane and shear moduli effectively act as penalty parameters (weakly) enforcing inextensibility and unshearability. In particular, for the strip used in figures 9 and 10, these ratios are approximately 2.12×10^6 and 6.3×10^5. Hence, both the developable strip and Cosserat plate theories effectively coincide when modelling the bending dominated deformations involved in the construction of Möbius strips. The super-linear dependence of the predicted energies on the width is clear from the plot. This feature is in contrast to the linear dependence predicted by the rod model, which, as discussed previously, we expect from the width-independence of the predicted solutions. We also note that despite its poor predictions for the shapes of strips seen in figure 10, figure 12*b* shows, perhaps surprisingly, that the rod model predicts lower energies than the Cosserat plate and developable strip models. This observation points at inadequacies of the rod model in accounting for energetic contributions from the kinematics involved in constructing Möbius strips.

Remarks 1. We conclude this section with a few remarks.

(i) It is not surprising that the plate-based developable strip and Cosserat models outperform the Kirchhoff rod model in predicting shapes and features of Möbius bands constructed from reasonably wide strips. These observations echo similar findings reported from recent studies on ribbon structures in [12,17], for instance. Significantly perhaps, the comparisons between experiments and model predictions conclusively add the canonical case of a Möbius strip to the list of examples that help distinguish rod- and plate-based models.

(ii) Simulations of the Cosserat plate theory, although new in the context of modelling Möbius strips, essentially confirm anticipated solution features [18,20]. Extensibility and shearability in the model were inconsequential in the current study involving bending dominated deformations. However, we expect them to be useful in more general investigations of ribbon structures (cf. [39]).

(iii) Applications of the developable strip theory in ribbon mechanics are motivated by the premise of its performance in predicting shapes of Möbius strips. Its comparison with experimental measurements provides unambiguous validation in this context.

(iv) The observations on the performance of the rod model identify quantitative shortcomings in modelling Möbius strips as rods with slender cross sections [16]. Nevertheless, we also note that the rod theory continues to be successfully used in modelling a variety of problems involving ribbon-like structures [21,40].

7. Concluding remarks

The two stereo vision-based techniques proposed in this article enabled us to undertake a detailed examination of a model system in ribbon mechanics. They represent a non-trivial departure from ubiquitous digital image correlation methods [26], which are ill-suited for measuring deformations involving large displacements and rotations. Both are readily accessible low-cost techniques that promise to be useful in the general context of visualizing and measuring complex deformations of slender elastic structures. The marker-based technique also seems appropriate for measuring dynamic deformations or ribbons.

An immediate consequence of the shape and deformation measurements of Möbius strip made possible by these techniques is a resounding endorsement of the geometric ideas underlying the developable strip model. Equally significantly, the measurements help chronicle deficiencies in modelling ribbons as rods with slender cross-sections. The Cosserat plate theory's efficacy for modelling Möbius strips shown here complements the study in [12]. The purpose of examining the theory here is not to advocate modelling Möbius strips or ribbons as plate structures. Rather, its validation shown here inspires confidence in adopting readily available simulation codes that implement algorithms approximating its predictions to study problems in ribbon mechanics. This is especially significant in light of the challenges that persist in using the developable strip model [22]. Specifically, owing to the choice of coordinates for deformed surfaces, it is necessary to account for singularities in solutions at locations where the centreline curvature vanishes. Simulations of the developable strip model from [18] reproduced here exploit *a priori* knowledge of these singular points. It remains to be seen whether the model can be used in problems where the existence or locations of such singularities are not known beforehand, or may even change during loading. The Cosserat plate theory circumvents these issues entirely.

Finally, we hope that the experimental data made available with this article will help accelerate the development of dedicated ribbon models. For, irrespective of the possibilities, one thing is clear—the problem of predicting the shape of a Möbius strip will remain a litmus test that any such model will need to pass.

Data accessibility. A dataset containing documented sets of files with experimental measurements and model simulations is provided at this link: https://doi.org/10.6084/m9.figshare.14479398.

Authors' contributions. A.K.: Mechanical modelling, finite-element simulation, numerical simulations; P.H.: Sample preparation, experimental measurements, validations; D.B.: Fabrication, experimental measurements; R.R.: Conceptualization, mechanical modelling, finite-element software development, measurement techniques, manuscript preparation and funding. All authors gave final approval for publication and agree to be held accountable for the work performed therein.

Competing interests. We declare we have no competing interests.

Funding. Science and Engineering Research Board (SERB, India) Early Career Research Award ECR/2017/000346 and Core Research Grant CRG/2020/003641.

References

1. Pickover C. 2007 *The Möbius strip: Dr. August Möbius's marvelous band in mathematics, games, literature, art, technology, and cosmology*. New York, NY: Basic Books.
2. Prevos P. 2018 *The Möbius strip in magic: a treatise on the Afghan bands*. Kangaroo Flat, Australia: Third Hemisphere Publishing.

3. Seiner J, Backley F, Gilinsky M. 1998 Screws, propellers and fans based on a Möbius strip. In *4th AIAA/CEAS Aeroacoustics Conf., Toulouse, France, 2–4 June 1998*. (doi:10.2514/6.1998-2260)
4. Caetano E, Freire V, Dos Santos S, Galvao D, Sato F. 2008 Möbius and twisted graphene nanoribbons: stability, geometry, and electronic properties. *J. Chem. Phys.* **128**, 164719. (doi:10.1063/1.2908739)
5. Han D, Pal S, Liu Y, Yan H. 2010 Folding and cutting DNA into reconfigurable topological nanostructures. *Nat. Nanotechnol.* **5**, 712–717. (doi:10.1038/nnano.2010.193)
6. Tanda S, Tsuneta T, Okajima Y, Inagaki K, Yamaya K, Hatakenaka N. 2002 A Möbius strip of single crystals. *Nature* **417**, 397–398. (doi:10.1038/417397a)
7. Wakabayashi K, Harigaya K. 2003 Magnetic structure of nano-graphite Möbius ribbon. *J. Phys. Soc. Jpn.* **72**, 998–1001. (doi:10.1143/JPSJ.72.998)
8. Ben Amar M, Pomeau Y. 1997 Crumpled paper. *Proc. R. Soc. Lond. A* **453**, 729–755. (doi:10.1098/rspa.1997.0041)
9. Gupta S, Saxena A. 2014 A topological twist on materials science. *MRS Bull.* **39**, 265–279. (doi:10.1557/mrs.2014.28)
10. Fosdick R, Fried E. 2016 *The mechanics of ribbons and Möbius bands*. Berlin, Germany: Springer.
11. Korte A, Starostin E, van der Heijden G. 2011 Triangular buckling patterns of twisted inextensible strips. *Proc. R. Soc. A* **467**, 285–303. (doi:10.1098/rspa.2010.0200)
12. Kumar A, Handral P, Bhandari D, Karmakar A, Rangarajan R. 2020 An investigation of models for elastic ribbons: simulations & experiments. *J. Mech. Phys. Solids* **143**, 104070. (doi:10.1016/j.jmps.2020.104070)
13. Bradski G. 2000 The OpenCV Library. Dr. Dobb's Journal of Software Tools.
14. Sadowsky M. 1929 Die Differentialgleichungen des Möbiusschen Bandes. *Jahresber. Dtsch. Math.-Ver.* **39**, 2.
15. Hinz D, Fried E. 2015 Translation of Michael Sadowsky's paper 'The differential equations of the Möbius band'. *J. Elast.* **1**, 19–22. (doi:10.1007/s10659-014-9491-4)
16. Mahadevan L, Keller J. 1993 The shape of a Möbius band. *Proc. R. Soc. Lond. A* **440**, 149–162. (doi:10.1098/rspa.1993.0009)
17. Huang W, Wang Y, Li X, Jawed M. 2020 Shear induced supercritical pitchfork bifurcation of pre-buckled bands, from narrow strips to wide plates. *J. Mech. Phys. Solids* **145**, 104168. (doi:10.1016/j.jmps.2020.104168)
18. Starostin E, van der Heijden G. 2007 The shape of a Möbius strip. *Nat. Mater.* **6**, 563–567. (doi:10.1038/nmat1929)
19. Moore A, Healey T. 2019 Computation of elastic equilibria of complete Möbius bands and their stability. *Math. Mech. Solids* **24**, 939–967. (doi:10.1177/1081286518761789)
20. Randrup T, Røgen P. 1996 Sides of the Möbius strip. *Arch. Math.* **66**, 511–521. (doi:10.1007/BF01268871)
21. Yu T, Hanna J. 2019 Bifurcations of buckled, clamped anisotropic rods and thin bands under lateral end translations. *J. Mech. Phys. Solids* **122**, 657–685. (doi:10.1016/j.jmps.2018.01.015)
22. Charrondière R, Bertails-Descoubes F, Neukirch S, Romero V. 2020 Numerical modeling of inextensible elastic ribbons with curvature-based elements. *Comput. Methods Appl. Mech. Eng.* **364**, 112922. (doi:10.1016/j.cma.2020.112922)
23. Wunderlich W. 1962 Über ein abwickelbares Möbiusband. *Monatsh. Math.* **66**, 276–289. (doi:10.1007/BF01299052)
24. Hartley R, Zisserman A. 2003 *Multiple view geometry in computer vision*. Cambridge, UK: Cambridge University Press.
25. Ma Y, Soatto S, Kosecka J, Sastry S. 2012 *An invitation to 3-D vision: from images to geometric models*, vol. 26. Berlin, Germany: Springer Science & Business Media.
26. Sutton M, Orteu J, Schreier H. 2009 *Image correlation for shape, motion and deformation measurements: basic concepts, theory and applications*. New York, NY: Springer.
27. Fiala M. 2009 Designing highly reliable fiducial markers. *IEEE Trans. Pattern Anal. Mach. Intell.* **32**, 1317–1324. (doi:10.1109/TPAMI.2009.146)
28. Olson E. 2011 AprilTag: a robust and flexible visual fiducial system. In *IEEE Int. Conf. on Robotics and Automation, Shanghai, China, 9–13 May 2011*, pp. 3400–3407. (doi:10.1109/ICRA.2011.5979561)
29. Garrido-Jurado S, Muñoz-Salinas R, Madrid-Cuevas F, Marín-Jiménez M. 2014 Automatic generation and detection of highly reliable fiducial markers under occlusion. *Pattern Recognit.* **47**, 2280–2292. (doi:10.1016/j.patcog.2014.01.005)

30. Geng J. 2011 Structured-light 3D surface imaging: a tutorial. *Adv. Opt. Photonics* **3**, 128–160. (doi:10.1364/AOP.3.000128)
31. Schwarz G. 1990 The dark side of the Moebius strip. *Am. Math. Mon.* **97**, 890–897. (doi:10.1080/00029890.1990.11995680)
32. O'Reilly O. 2017 *Modeling nonlinear problems in the mechanics of strings and rods: the role of the balance laws*. Interaction of Mechanics and Mathematics. Berlin, Germany: Springer International Publishing.
33. Love A. 2013 *A treatise on the mathematical theory of elasticity*. Cambridge, UK: Cambridge University Press.
34. Dias M, Audoly B. 2015 'Wunderlich, Meet Kirchhoff': a general and unified description of elastic ribbons and thin rods. *J. Elast.* **1**, 49–66. (doi:10.1007/s10659-014-9487-0)
35. Todres R. 2015 Translation of W. Wunderlich's 'On a developable Möbius band'. *J. Elast.* **119**, 23–34. (doi:10.1007/s10659-014-9489-y)
36. Simo J, Fox D, Rifai M. 1990 On a stress resultant geometrically exact shell model. Part III: computational aspects of the nonlinear theory. *Comput. Methods Appl. Mech. Eng.* **79**, 21–70. (doi:10.1016/0045-7825(90)90094-3)
37. Simo J. 1985 A finite strain beam formulation. The three-dimensional dynamic problem. I. *Comput. Methods Appl. Mech. Eng.* **49**, 55–70. (doi:10.1016/0045-7825(85)90050-7)
38. Starostin E, van der Heijden G. 2015 Equilibrium shapes with stress localisation for inextensible elastic Möbius and other strips. *J. Elast.* **119**, 67–112. (doi:10.1007/s10659-014-9495-0)
39. Kleiman D, Hinz D, Takato Y, Fried E. 2016 Influence of material stretchability on the equilibrium shape of a Möbius band. *Soft Matter* **12**, 3750–3759. (doi:10.1039/C5SM02188J)
40. Riccobelli D, Noselli G, DeSimone A. 2021 Rods coiling about a rigid constraint: helices and perversions. *Proc. R. Soc. A* **477**, 20200817. (doi:10.1098/rspa.2020.0817)